Vol. 08, No. 2 (2026) 689-698, doi: 10.24874/PES08.02.008

Proceedings on Engineering Sciences

www.pesjournal.net

# METHODS FOR PROCESSING GADANKI IONOSPHERIC INTERFEROMETER RADAR DATA FOR IMAGING

Timiti Vamsi Krishna
Ravindra Dhuli[1]

Received 10.12.2025.
Revised 06.04.2026.
Accepted 28.04.2026.

Keywords:

*Interferometry, Ionospheric irregularities, Equatorial electrojet, Cross-power spectrum, Angle of arrival, Doppler frequency, Radar imaging*

A B S T R A C T

*This paper provides an analysis of Gadanki ionospheric radar interferometer (GIRI) data and develop RTI images. The time series data analysis allows us to understand the EEJ irregularity. Initially an illustration on the radar set up of GIRI is presented. To make the data useful for processing the DC removal followed by the clutter removal also employed. This operation helps to remove speckle, thermal noise and interference. From each channel data, using the Fourier transform the power spectral density of the signal at each Doppler frequency is computed. Power spectral density added over all Doppler frequency gives the total signal power. Additionally, signal and noise power are computed. From those powers, detectability of the signals is expressed in terms of signal to noise ratio (SNR) for individual frame. Accumulation of each frame SNR as a function of range and time provides us an RTI plot. Here SNR is indicating the intensity. These Figures illustrate an approximation of EEJ and corresponding RTI plots consisting of small and intermediate scale irregularities obtained for individual receiving channels. A discussion on radar interferometry is presented with the evaluation of cross power spectrum and the ability to identify the irregularity is also presented.*

© 2026 Published by Faculty of Engineering

## 1. INTRODUCTION

Atmospheric observations using radar gained significant attention from various research communities. They are successful in measuring several parameters like wind velocities, temperature, pressure, humidity, electron density distribution in the evolution of ionospheric irregularities, directional flow of the turbulence and stability in the dynamics of the atmospheric layers etc. Here we are interested in ionospheric irregularities, which disturb reliable navigation and satellite communication systems.

Hence an accurate characterization of ionosphere is required. From past several decades, ground based radars are used to investigate aforementioned phenomenon in ionospheric E, F region using interferometry technique. It is the technique, which synthesize large aperture in space from the small distributed apertures on the ground. To measure the inclination of Geo-magnetic field R. F. Woodman (Woodman, 1971) introduced the radar interferometry, where the received backscattered signal voltages are directly cross-correlated. With an extension of baselines along east - west directions, D. T. Farley and team, proposed new radar interferometry technique to investigate the ionospheric irregularities, later E. Kudeki

1 Corresponding author: Ravindra Dhuli
Email: ravindra.d@vitap.ac.in

and team continued the same technique to probe ionospheric F-region irregularities (Farley et al., 1981; Kudeki et al., 1981). To measure field aligned irregularities (FAI), we need backscattered signal spectrum. Cross spectrum of different receiving channels is used for identifying the nature of the irregularity. Each Doppler frequency within the spectrum determines the localization of the echoing center within the radar beam width and corresponding values represents the mean angular position of the irregularity along east-west plane. Further, this technique used for monitoring the wind profile and clean air turbulence applications using spaced antenna (SA) mode in post beam scanning (PBS) method (Röttger & Ierkic 1985). To overcome the drawbacks in PBS, anew method post statistic steering (PSS) proposed by Kudeki and Woodman (1990). It is almost equivalent to beamforming technique and useful for imaging the irregularity structures with in radar field of view (FOV) (Kudeki & Sürücü, 1991). First imaging of ionospheric FAI in the electrojet using CRI was carried out by Kudeki and Sürücü (1991). Later imaging the irregularities during day and night scenarios carried out by D. L. Hysell using radar system located at Jicamarca with different configuration (Hysell, 1996). Palmer et al. (1998) developed the brightness distributions in horizontal and vertical cross-sections using MU radar. Hysell and Chau developed imaging of EEJ, spread F scenario using radar located at Jicamarca with various configurations (Hysell & Chau, 2002, 2006, 2023). Rodrigues carried out the spread F imaging using $São$ Luis located in Brazil (Rodrigues et al., 2012). These works motivated us to explore the imaging possibilities to observe the irregularities using Gadanki ionospheric radar interferometer (GIRI) at low latitude region.

We discussed the experimental setup of GIRI system in section 2 and analysed the time series data in section 3. In section 4, we presented identification of their regularity type. Conclusion is discussed in section 5.

**Notation**: The symbols $(.)*$, $\langle . \rangle$ and $(*)$ denote, complex conjugate transpose, the ensemble average and convolution operator, respectively. Similarly, uppercase boldface letters represent matrices.

## 2. EXPERIMENTAL SETUP

A 30 MHz, GIRI is located at National Atmospheric Research Laboratory (NARL), India to probe the low latitude ionospheric irregularities. A 160 two element yagi-uda antennas are arranged in a 20 × 8 array format, with an inclination of 14° from the horizontal plane to project the beam in transverse to the earth's magnetic field. Figure 1 represents the diagram of the experimental setup of the GIRI and each '*' indicates yagi-uda antenna element. Each column (along east-west direction) of the array contains 8 antenna elements, separated along north-south direction with a distance separation of $0.7\lambda$. Similarly, each row (north-south direction) of the array contains 20 antenna elements separated with a spacing of $0.56\lambda$ along east-west direction. Here $\lambda$ is the operating wavelength equal to 10 m. All the array elements divided into five channels of each containing 4 columns along east- west direction. Each column of the antenna array is considered as a 7.5 kW solid-state transmit-receive (TR) module. Such twenty TR modules radiate a total peak power of 160 kW. RF and switching circuit helpful in distributing power from the exciter across all the channels in transmit mode and combine backscattered signal received in each channel and forwarding to its backend receiver unit in receiving mode. Each channel is connected to its individual direct digital receivers (DDR). A separate DDR also available for mixing all channel signal. GIRI system can operated in both Doppler beam swinging (DBS) and spaced antenna (SA) mode. During SA interferometry mode, all five DDR's receive signals from the corresponding channels. It is useful for the irregularity imaging applications by connecting phase-centers of each channel with the help of collinear baselines. The primary baseline lengths between phase-centers represented as $d_0 = 2.24\lambda$. Baselines related to the main antenna array only considered for the experiment. When GIRI operated in DBS mode, sixth DDR receives the signals from all channels for wind profiling application. Beam width of the GIRI array is 4.5° in east west and 9° in north-south direction (Patra et al., 2014; Srinivasulu et al., 2013).

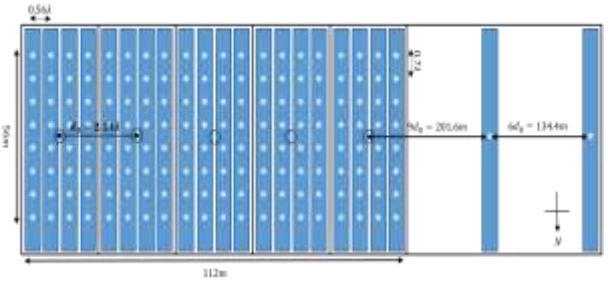


**Figure 1.** Experimental setup of the GIRI system

## 3. RANGE TIME INTENSITY PLOT GENERATION USING TIME SERIES DATA

Here in this paper electrodynamics of the irregularities, patchy eddy structures elongated in the altitude of E and $E_s$ (Sporadic-$E$ layer) and $F$ region during daytime have been investigated. The data was collected during the GIRI system operated in SA interferometry mode. At the time of data record, raw data stored in time series format for large number of cycles. Each cycle contains large number of frames. A minute data snapshot in the cycle is referred as a frame, it contains uniformly sampled complex baseband signal. Each channel contains separately received time series signal across all range bins with the number of FFT sample points, Figure 2 illustrates the backscattered signal received at the channel 1 first frame $I, Q$ data components at 99.6 km.
Here number of range bins (nrgb) denoted by $h \in \{1, 2, 3, \ldots 80\}$. Number of nfft sample points number of FFT (nfft) denoted by $l \in \{1, 2, 3 \ldots 512\}$.

Representation of the $M^{th}$ channel complex baseband signal interms of inphase and quadrature phase can be written as

$$r_M(h,l) = r_I(h,l) + j\ r_Q(h,l). \quad (1)$$

Where j = $\sqrt{-1}$. The time series data obtained in each frame with a range resolution of 1.2 km in time duration of 2.8672 sec. To make optimal use of data for detecting temporal evolution of irregularity structure using a range time intensity (RTI) plot, some signal processing operations performed in a sequence as discussed below.

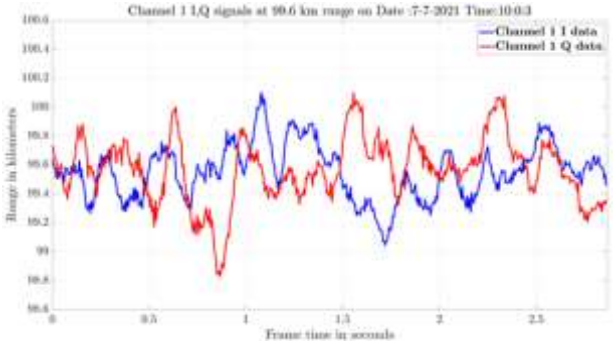



**Figure 2.** I and Q signal data components of first frame channel 1 raw data at 99.6 km range.

### 3.1 Removal of direct current (DC) component

Time series data obtained with individual channel data across all range bins of a frame. DC is also known as the non-time varying component. Removing the mean value of each range bin in equation (1) from each sample point of the corresponding channel range bin provides the DC component free data. Removal of non-time varying component from the complex baseband signal obtained at each range bin sample point of the corresponding channel helps to find out time varying signal component. Accurate information about the target detection and tracking provided by the time varying signal component. This helps when the interference obtained from the strong clutter. Similarly, in case of non-time varying component provides ambiguous information about the moving target so that DC removal is necessary in the initial stage of data processing.

$$\widetilde{r_M}(h,l) = \frac{1}{nfft}\left(\sum_{l=1}^{nfft} r_M(h,l)\right) \quad (2)$$

$$\overline{r_M}(h,l) = r_M(h,l) - \widetilde{r_M}(h,l). \quad (3)$$

where $\widetilde{r_M}(h,l)$ is the mean value of the range bin h, computed over l samples for corresponding channel $M$. $\overline{r_M}(h,l)$ is the representation of the $M^{th}$ channel DC component free complex baseband signal across all range bins of sample points. Note that nfft is the number of fft sample points.

### 3.2 Clutter removal

Clutter is an object which generates the undesirable radar return signal that interferes with the radar operations. To remove the undesired effect obtained because of slowly moving clutter a three-point averaging (moving average) is required. This operation helps to remove background noise or interference obtained (Anandan et al., 2005). Data processing operations like moving target indicator (MTI) and Kalman filtering are suitable for fastly moving clutters (Sinha et al., 2017).

$$\bar{r}_M^L(h,l) = \frac{1}{L}[\overline{r_M}(h,l-1) + \overline{r_M}(h,l) + +\overline{r_M}(h,l+1)] \quad (4)$$

where $L$ = 3. Dropping the suffixes and subscripts for a moment to simplify the notation,

$$r(h,l) = \bar{r}_M^L(h,l). \quad (5)$$

### 3.3 Power computation

In any independent channel, after removing DC and clutter component effects from each channel data, multiplying the Fourier transform of each range bin signal with its complex conjugate in corresponding receiving channel provides the power spectral density of the signal at each Doppler frequency. Power spectral density added over all Doppler frequency gives the total signal power, $P$ of the corresponding range bin of the respective channel. Here $\Omega_l$ is the discrete frequency value in frequency domain. In the entire window of range bins last range bin total power is considered as noise level due to longer propagation, clutter etc., Removing noise power from signal power in each range bin provides the desired signal power in the range. Here, signal power denoted with $P_s$ and noise power denoted with $P_n$.

$$P(h,\Omega_l) = \sum_{l=1}^{nfft} r(h,\Omega_l)\, r^*(h,\Omega_l),$$

$$= \sum_{l=1}^{nfft} |r(h,\Omega_l)|^2. \quad (6)$$

$$P_n(h = nrgb, \Omega_l) = \sum_{l=1}^{nfft} |r(h = nrgb, \Omega_l)|^2\ . \quad (7)$$

$$P_n\ =\ \sigma_n^2\ ;$$

$$P_s(h,,\Omega_l) = \sum_{l=1}^{nfft} [P(h,\Omega_l) - \sigma_n^2\ ]. \quad (8)$$

### 3.4 SNR computation

Generally, atmospheric coherent scatter radars are used to observe the unattended plasma irregularities from ground. Atmospheric radar detectability is completely depending on the backscattered signals received at the individual receiving channels. From the obtained DC and clutter free components of raw data, signal and noise power computation is possible. From those powers, detectability of the signals is expressed in terms of signal to noise ratio (SNR) for individual frame. Accumulation of each frame SNR as a function of range and time provides us an RTI plot. Here SNR is indicating the intensity (Woodman, 1997).

$$SNR = 10 \log\left(\frac{P_s(h,,\Omega_l)}{P_n(h,,\Omega_l)}\right). \qquad (9)$$

Figure 3 shows the extremely rare approximation of EEJ and corresponding RTI plots consisting of small and intermediate scale irregularities obtained for individual receiving channels. Range resolution in the each RTI plot is 1.2 km and they cover the temporal evolution of irregularity that approximately spread over 3-10 km dynamic range in east-west direction. In this paper, raw data is collected during EEJ condition and processed to generate RTI plot with a time resolution of 2.8672 seconds from day time 10:00:03 to 10:41:36. RTI plot is similar to the slit-camera image, so that it is also called as pseudo image. The obtained plots show the turbulent activity of the FAI observed in terms of both SNR, time and range extent. Intensity levels measured with the colour bars ranging from -20 dB to 20 dB. We consider the temporal evolution of irregularity only for the signal - component intensity levels greater than 30 dB above noise level (Hildebrand & Sekhon, 1974). The above mentioned assumption helps to know about the state of flowing medium in the scattering volume.

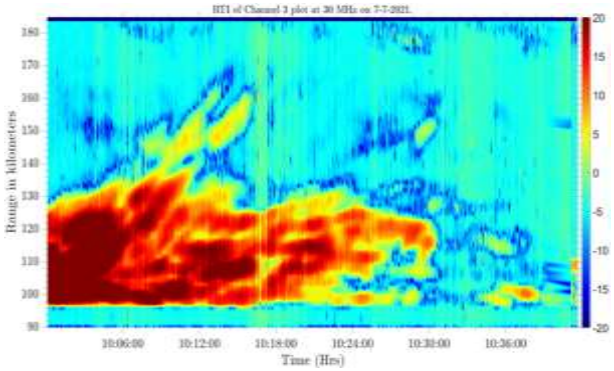



**Figure 3.** Range Time Intensity plot obtained from backscatter signal received at Channel 3

## 4. RADAR INTERFEROMETRY TECHNIQUE

During the experiment the 30 MHz, coherent GIRI five channel antenna array acts as a transmitter to radiate the beam in transverse to the earth magnetic field it receives the echo signals from irregularities at each individual receiving channels, which are arranged along east – west direction. Multiple spatially separated antennas used for examining the backscattered signals obtained from scattering volume with in radar beam width is known as SDI (Palmer et al., 1998). Figure 4 is illustrating SDI. For easy understanding of spatial domain interferometry (SDI) and to perform mathematical analysis between received backscattered signal, we are initially illustrating two receiving channels in the Figure 4.

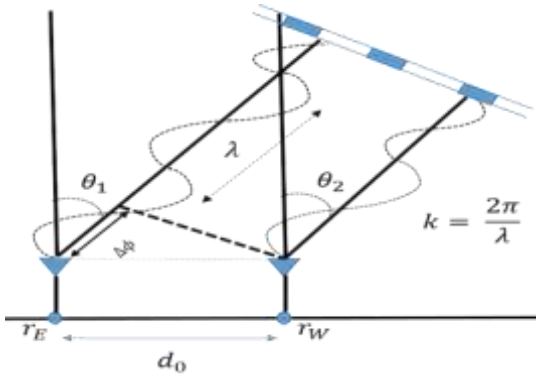



**Figure 4.** Diagram of the Spatial domain interferometry

Consider small scale irregularities presented with in the radar beam width at particular range. Such irregularities are strongly field aligned along the Earth's magnetic field and responsible for the backscatter of the radar transmitted electromagnetic waves. These irregularities are located at an angular position of $\overline{\theta_\omega}$ in east– west plane and moving with a radial velocity of $v_r = \frac{f_d \lambda}{2}$, either towards (+) or away (-) from the radar, where $f_d$ is the Doppler frequency, $\lambda$ is the radar wavelength. The antenna beam width and pulse length determines the size of the scattering volume. For the first time studying the EEJ irregularity scenario to identify its type and velocity from GIRI radar has been initiated in this paper. Parameters using while conducting the experiment are having a pulse length of 8 $\mu sec$, inter-pulse period is of 1400 $\mu sec$ with number of coherent and in-coherent integrations of four and one, respectively allow us to produce: (i) a range resolution of 1.2 km, with 80 range bins sample over 90 - 184.8 km and (ii) Doppler shifts up to ± 89.285 Hz without aliasing. Radar backscatter signals inferred as the spectrum of plane waves arriving from small scale irregularity at a large distance (location is behind the far-field or Fraunhofer limit). Such backscattered voltage signal received at the east side of receiving channel can be written as

$$r_E(t) = \sum_i A_i(\omega)\, e^{j(\phi_i + \omega t)}, \qquad (10)$$

where $A_i$ is the amplitude and $\phi_i$ is the $i^{th}$ random phase angle of the small scale irregularity. $\phi_i$ is uniformly distributed over the interval $[0, 2\pi]$. Here, $\omega = 2\pi f$ refers to the angular frequency of the echo signal, where

$f$ is the Doppler shift. Fourier transforming a short portion of the data gives

$$r_E(\omega) = \sum_i A_i(\omega)\, e^{j(\phi_i)} \quad (11)$$

Assuming $A_i(\omega)$ slowly varies with time. Similarly, Fourier transform of the voltage signal received at the west-side receiving channel in frequency domain can be written as

$$r_W(\omega) = g \sum_i A_i(\omega)\, e^{j(\phi_i - kd_0 \sin(\theta_i))}, \quad (12)$$

Here $k$ is the wavenumber vector $\frac{2\pi}{\lambda}$ and $\sin(\theta_i)$ is the angular position of the $i^{th}$ small scale irregularity, here $\sin(\theta_i)$ replaced with $\theta_i$. The term $g$ represents the gain, it will dropdown while performing calculations. Here $d_0$ is the primary base line length between the receiving channels (Farley et al., 1981).

$$r_W(\omega) = g \sum_i A_i(\omega)\, e^{j(\phi_i - \Delta\phi_i)}. \quad (13)$$

Phase angle of the received signals $\phi_i$ are independent on each other and uniformly distributed over $[0, 2\pi]$, the ensemble average (equivalent to spatial or temporal averaging) is also zero. Here $\Delta\phi_i = kd_0 \sin(\theta_i)$ is the delay in phase of the receiving signal at west side sensor.

$$\langle e^{j\phi_i} \rangle = 0.$$

The fundamental concept behind correlating the received radar backscatter signals is to infer the moments of arrival angle distribution, which helps to examine the irregularity structure of the scattering medium in the direction perpendicular to the radar beam.

$$\langle r_E(\omega)\ r_W^*(\omega) \rangle = \left( g \sum_i A_i^2 \right) \langle e^{jkd_0\theta_i} \rangle \quad (14)$$

Normalized cross power spectrum is given by,

$$V_{EW}(\omega) = \frac{\langle r_E(\omega)\ r_W^*(\omega) \rangle}{\sqrt{\langle |r_E(\omega)|^2 \rangle \langle |r_W(\omega)|^2 \rangle}} \quad (15)$$

an equation we obtain

$$V_{EW}(\omega) = \langle e^{jkd_0\theta_i} \rangle \quad (16)$$

Assuming phase $\theta_i$ have gaussian distribution with mean $\overline{\theta_\omega}$ and variance $\sigma_\omega^2$ , according to the characteristic function, equation (16) can be re-written as

$$V_{EW}(\omega) = \langle e^{jkd_0\overline{\theta_\omega}} \rangle \left[ e^{-\frac{1}{2}k^2 d_0^2 \sigma_\omega^2} \right]. \quad (17)$$

In case of multiple small scale irregularities, backscattering signals with its own Doppler shift, mean position $\overline{\theta_i}$ and angular spread $\sigma_\omega$ equation (17) is modified with summation over the all Doppler shifts. It is important to know about the cross spectra $V_{EW}(\omega)$, in (15). Individual power spectra $|r(\omega)|^2$ of weakly received signal from small-scale irregularity at different frequencies result in large normalized cross spectra. Similarly, the power spectra of strongly received signal from large-scale irregularity or multiple different regions within radar scattering volume result in small normalized cross spectra at different frequencies. Random receiver or cosmic noise provides weak cross spectra not because of weak signal, because there is no phase relation between the two signals (Gruber, 1997). During EEJ condition weakest components are frequently observed above the noise level. From equation (15) the phase of the cross spectrum relates with the angle $\overline{\theta_i}$, maximum baseline length d and also depends on altitude $H$. At an altitude $H$, the distance $\delta x$ corresponds to the phase difference $\delta\phi_i$ is

$$\delta x = H \frac{\delta\phi_i}{kd} \quad (18)$$

GIRI system has the spacing $d = 8.94\lambda$, resutling in,

$$\delta x = 0.01777 \times H \times \delta\phi_i \quad (19)$$

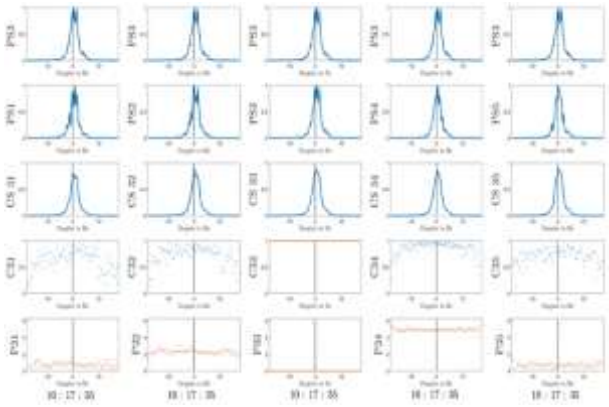


**Figure 5.** Top two rows represent the power spectrums labelled with PS, third row is the corresponding cross spectrum labelled with CS, fourth row is the coherence labelled with C and fifth row is the phase labelled with P of channel 3 with respect to all channels at the range bin 99.6 km on 7th July 2021.

Note that 5° phase difference corresponds to 154.389 m displacement at 99.6 km altitude. The data presented here was collected on around daytime in 7th July 2021. During the experiment radar was positioned vertically and projected the beam transverse to the earth's magnetic field. All eighty range bins sampled and integrated for a time period ≈ 29 sec. From the equation (15), we can calculate the individual power spectrums and normalized cross power spectrums and corresponding phase difference among any two of receiving channels.

Equation (15) Coherence (visibility) is the key factor to estimate the brightness distribution in coherent radar imaging (CRI) from the measured visibility samples (coherence). Figure 5 shows the relation between signal received at channel 3 and all receiving channels at the range 99.6 km. It illustrates the representation of small sample result.

Top two rows in the Figure 5 represents the power spectrums and third row represents the cross power spectrum obtained between receiving channels. Fourth row represents the normalized cross power spectrum and fifth row represents the phase difference between corresponding ends of the receiving channels. The cross spectra normalized in equation (15) has magnitude known as coherence$|V_{EW}(\omega)|$ and the phase angle $\angle V_{EW}(\omega) \approx \Delta\phi_i$. $|V_{EW}(\omega)|$ values spread over [0, 1], and phase angles $\Delta\phi_i$. are spread over $[0, 2\pi]$ radians. Each tick mark on the vertical axis of phase is covering 30° or $\frac{\pi}{6}$ radians. Cross power spectrum classifies the irregularity type. Increase in phase angle of subsequent sample indicates the displacement of the scattering region towards east. At time 10:17:35 in supports the same scenario at 99.6 km. A 20° change in the phase angle at an altitude corresponds to a displacement of 648.7 m. Here, spectral peaks spread over Doppler shifts ± 89.285 Hz. If the spectral peak located towards positive Doppler shift ($f_d$) values corresponds to westward, down going irregularity. If the spectral peak is located towards negative Doppler shift (-$f_d$) values corresponds to eastward, up going irregularity .

### 4.1 Equatorial electrojet type and discussion

EEJ is a worldwide phenomenon that contains a narrow ribbon like currents confined to E-region (especially in between 90 - 110 km), flowing along the earths geo-magnetic equator. EEJ is a day and night phenomenon. It is primarily driven by dynamic action of neutral winds, solar radiation, earth magnetic field variation. This tends to form unique electric and magnetic field conditions within the equatorial latitudes of ±3◦.Very thin, anomalous, highly dense ionization scattering layers occurred at > 120 km of E-region at equatorial latitude called as sporadic $E$-region ($E_s$). Both $E$ and ($E_s$) have different generating mechanisms as well as characteristics. In this paper an attempt has done by analysing the radar return data during day time, to know the information related to E-region EEJ. EEJ in E-region is associated with two types of irregularities, known as strong plasma drift instability (SPI) or type I echoes and gradient drift instability (GDI) or type II echoes (Woodman & La Hoz, 1976).

Characteristics of the type I echoes are (i) They are combination of two stream irregularities observed in EEJ region during day-time, (ii) The reason for the two stream irregularities is relative drift between electrons and ions due to potential electric field, (iii) Narrow spectrum with a clear Doppler shift corresponds to ion-acoustic velocity (few tens to several hundred meters per second), (iv) Highly coherent in nature, (v) Phase velocities of the type I irregularities have a component in the direction of the electron flow, usually electron flow is westward (Eastward) during day-time (night-time). The Doppler shift does not depend on the zenith angle; it indicates irregularities are advecting with the electron flow, besides it irregularity is saturated near ion-acoustic velocity. Characteristics of the type II echoes are (i) compared to type I echoes Doppler shift is very low, similarly ion acoustic velocity is also very low. (ii) Spectrum width is much broader than type I echoes (iii) type II echoes are formed from GDI due to steepest gradients in plasma irregularities (iv) less coherence in nature (v) phase velocity of type II echoes depends on the zenith angle and proportional to the drift velocity (Kudeki et al., 1981).

To analyse the type of irregularity consider the best range bin in EEJ region ($E$ - region ) by observing the RTI plots developed among any two channels. Thus we chose $9^{th}$, $12^{th}$, and $16^{th}$ range bins to examine EEJ irregularity among channel 3 and channel 4. Spectral data sampled at three different altitudes at each of three distinct times are illustrated in Figures 6, 7, and 8 as case I, case II and case III. First set of data contained in case I, obtained from the bottom part of the EEJ measured at three different intervals separated with 5.74 sec.

Figures 6 represent corresponding spectral characteristics of the received signals between channel 3 and 4 at range bin 99.6 km. First row contains a narrow peak cross power spectrum near zero Doppler shift. It is the indication of low Doppler velocity component. Second row contains the coherence, it is maximized near zero Doppler shift and continued even the cross power spectrum seems to be vanished. The reason for this is signal component is far above the noise level. Equivalent phase of the data is highly organized for high coherence near zero Doppler shift, and randomly distributed at all other Doppler shifts. The above all specifications supports that first set of data belongs to the type II EEJ irregularity. It implies turbulence of the gradient drift instability inside the scattering volume, is strongly field aligned and moving slowly. Here, signal is coming from the side by side locations of the highly localized region in the scattering volume. Phase points of the spectrum are highly arranged for Doppler shifts having large coherence and in other case phase points are randomly distributed. The peak value of the cross-power spectrum is at the positive Doppler shift $f_d$ gives negative Doppler velocity $v_r = \frac{-f_d \lambda}{2}$. It means irregularity at the lower altitude of EEJ is moving towards down, westward.

Similarly Figures 7, 8, contains three subsequent time interval observations at the middle 103.2 km and top portion 108 km of altitudes in the EEJ. The cross power spectrum is centred near negative side of Doppler shift at middle and completely shifted at top altitude is observed. The peak value of the cross-power spectrum is at the

negative Doppler shift ($f_d$) gives positive Doppler velocity $v_r = \frac{-(-f_d)(\lambda)}{2}$. When the cross power spectrum peak is shifted from positive to the negative Doppler shift according to the height, a decrease in the phase was observed. It implies that localized position of the echoing region is gradually moving towards east.

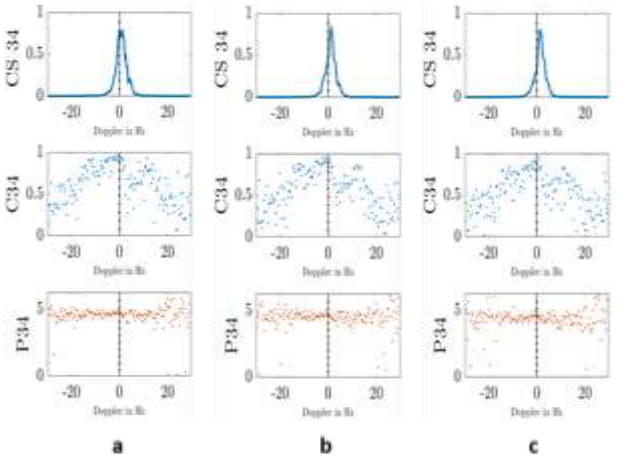



**Figure 6.** In Case I, (**a**) 10: 12 : 50 , (**b**) 10 : 12 : 56 , (**c**) 10 : 13 : 01 are sub figures contain cross power spectrum in top row, coherence in the middle row and the phase difference in the bottom row. These results are generated at height 99.6 km (9th range bin) at multiple intervals of time separated by ≈ 6 sec on 7th July 2021 during EEJ condition, from the signals received between channels 3 and 4

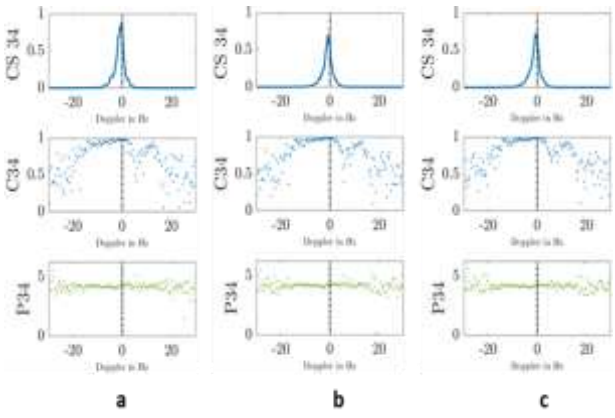



**Figure 7.** In Case II, (**a**) 10: 12 : 50 , (**b**) 10 : 12 : 56 , (**c**) 10 : 13 : 01 are sub figures contain cross power spectrum in top row, coherence in the middle row and the phase difference in the bottom row. These results are generated at height 103.2 km (12th range bin) at multiple intervals of time separated by ≈6 sec on 7th July 2021 during EEJ condition, from the signals received between channels 3 and 4

So different regions with phase variations in both sides of zero Doppler shift indicates up-going and down-going echoes are in two different regions in the same scattering volume. Multiple spectral peaks in cross spectrum was obtained because of spatial averaging. Among a number of unknown parameters in non-linear least square fitting method, linear least squares fitting might have applied iteratively to linear the form of function until the required convergence attained. To get best phase difference value on the curve fit, we can estimate the best phase difference $\Delta\widehat{\phi}_i$. Finding the residual $\Delta\phi_i - \Delta\widehat{\phi}_i$ provides the best goodness of fitting phase difference value $\Delta\phi_i$.

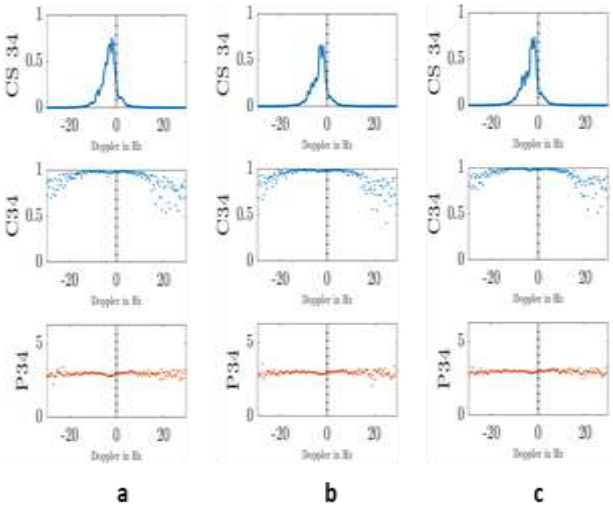



**Figure 8.** In Case III, (**a**) 10: 12 : 50 , (**b**) 10 : 12 : 56 , (**c**) 10 : 13 : 01 are sub figures contain cross power spectrum in top row, coherence in the middle row and the phase difference in the bottom row. These results are generated at height 108 km (16th range bin) at multiple intervals of time separated by ≈ 6 sec on 7th July 2021 during EEJ condition, from the signals received between channels 3 and 4

**Table 1**. Best phase observed in all three cases using non-linear least square curve fitting in phase

| Range in Km | 10:12:50 $\Delta\phi_1$ | 10:12:56 $\Delta\phi_2$ | 10:13:51 $\Delta\phi_3$ |
|---|---|---|---|
| Case I 99.6 Km | 1.488 $\pi$ | 1.447 $\pi$ | 1.440$\pi$ |
| Case II 103.2 Km | 1.337 $\pi$ | 1.344 | 1.3271 |
| Case III 108 Km | 0.94 $\pi$ | 0.94 $\pi$ | 0.93 $\pi$ |

Table 1 shows the corresponding phase differences at three time instances obtained for all the three cases discussed above.

## 4.2 Non-linear least square curve fitting in phase of EEJ

By observing the phases and arrival angles in the subsequent set of data frames, one can find the drift rate similar to ion-acoustic velocity. Using $v_\theta = h\frac{d\theta_i}{dt}$, where $v_\theta$ is the rate of change of Angle of arrival (AOA) with respect to the time at range $h$. Angular velocity of the gradient drift instability in the background can be estimated by measuring the phase angle of the discrete scattering source in the echoing region with respect to time. Phases are randomly distributed and if we consider

mean phase angle it will be zero due to Gaussian distribution. Due to that it is necessary to fit a curve among highly organized phase difference angles, which have maximum coherence value ≥ 0.7 at all Doppler shifts.

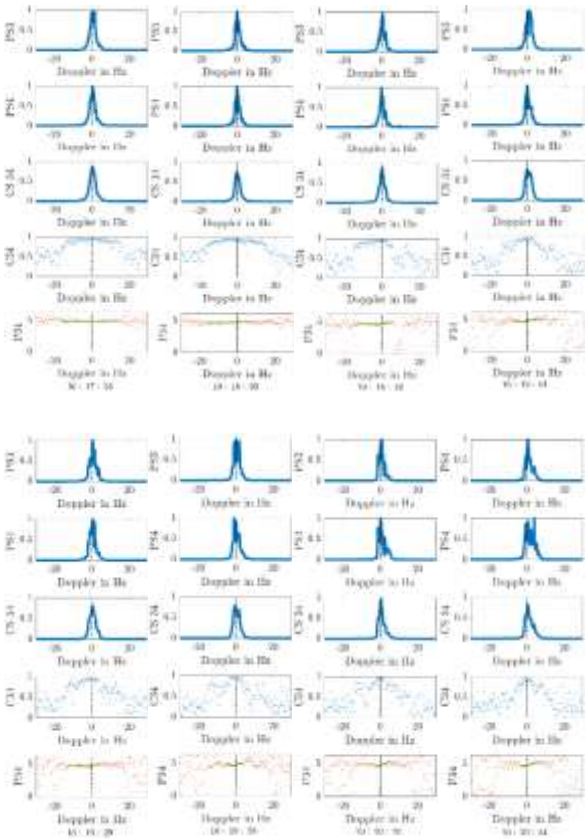


**Figure 9.** Each power spectrum column averaged over 28 sec of time and separated by 28 sec (≈ 10 frame). Power spectrums labelled with PS in first two rows, cross power spectrum labelled with CS in third row, coherence labelled with C and phase angle with curve fitting labelled with P at range bin 99.6 km in fourth and fifth rows, respectively. Green colour discrete line is the curve.

Non-linear least square curve fitting used over the discrete phase points, which obeyed the coherence condition. Non-linear least square curve fitting used over the discrete phase points, which obeyed the coherence condition. Figure 9 represents the spectral coherence data and curve fitting in phase data with first order non-linear least square method. By choosing the best phase, difference solution having ≈ low residual value helps to compute AoA of the echo signal coming from the scattering region. Mathematical representation for velocity from the AoA as follows

$$\theta_i = \sin^{-1}\left(\frac{\Delta\phi_i}{kd_0}\right) \tag{20}$$

$$v_\theta = h \times \frac{d\theta_i}{dt} \tag{21}$$

Figure 10 illustrates that the velocity of the GDI in EEJ at 99.6 km for shorter duration of time. Spectral peak appearances of the cross power spectrum in Figure 10 related to the polarity of the angular or transverse velocity through angle of arrival variation. Here, angular velocity approximately bounded in between ± 100 m/s (Briggs & Vincent, 1992).

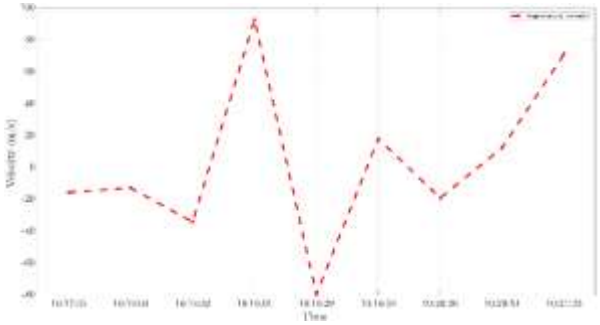


**Figure 10.** Velocity computation from the angle of arrival at the 99.6 km (9th range bin) during daytime EEJ

## 4. CONCLUSION

The GIRI system, with multi-channel baselines collinearly connected in SA interferometry mode provides a means to study the low latitude ionospheric irregularities and turbulence. The time series data is analysed to obtain cross power spectrum and identify the type of EEJ irregularities. Further from the phase information, AoA and angular velocity also evaluated.

**Acknowledgement:** The data is provided by National Atmospheric Research Laboratory (NARL), Gadanki, Department of Space, Government of India. The authors would like to thank the director Dr. A. K. Patra, Dr. M. Durga Rao, Dr. P. Pavan chaitanya, Mr. K. M. V.Prasad and other scientists and staff from NARL for their invaluable technical support.

## References:

Anandan, V. K., Balamuralidhar, P., Rao, P. B., Jain, A. R., & Pan, C. J. (2005). An adaptive moments estimation technique applied to MST radar echoes. *Journal of Atmospheric and Oceanic Technology*, *22*(4), 396–408. https://doi.org/10.1175/jtech1696.1

Briggs, B. H., & Vincent, R. A. (1992). Spaced-antenna analysis in the frequency domain. *Radio Science*, *27*(2), 117–129. https://doi.org/10.1029/91rs03051

Farley, D. T., Ierkic, H. M., & Fejer, B. G. (1981). Radar interferometry: A new technique for studying plasma turbulence in the ionosphere. *Journal of Geophysical Research Atmospheres*, *86*(A3), 1467–1472. https://doi.org/10.1029/ja086ia03p01467

Gruber, M. H. J. (1997). Statistical Digital Signal Processing and Modeling. *Technometrics*, *39*(3), 335–336. https://doi.org/10.1080/00401706.1997.10485128. https://doi.org/10.2307/1271141

Hildebrand, P. H., & Sekhon, R. S. (1974). Objective determination of the noise level in doppler spectra. *Journal of Applied Meteorology*, *13*(7), 808–811. https://doi.org/10.1175/1520-0450(1974)013

Hysell, D. L. (1996). Radar imaging of equatorialFregion irregularities with maximum entropy interferometry. *Radio Science*, *31*(6), 1567–1578. https://doi.org/10.1029/96rs02334

Hysell, D. L., & Chau, J. L. (2002). Imaging radar observations and nonlocal theory of large-scale plasma waves in the equatorial electrojet. *Annales Geophysicae*, *20*(8), 1167–1179. https://doi.org/10.5194/angeo-20-1167-2002

Hysell, D. L., & Chau, J. L. (2006). Optimal aperture synthesis radar imaging. *Radio Science*, *41*(2). https://doi.org/10.1029/2005rs003383

Hysell, D. L., & Chau, J. L. (2023). Aperture synthesis imaging of ionospheric irregularities using Time Diversity MIMO radar. *Radio Science*, *58*(9). https://doi.org/10.1029/2023rs007765

Kudeki, E., Fejer, B. G., Farley, D. T., & Ierkic, H. M. (1981). Interferometer studies of equatorial F region irregularities and drifts. *Geophysical Research Letters*, *8*(4), 377–380. https://doi.org/10.1029/gl008i004p00377

Kudeki, E., & Sürücü, F. (1991). Radar interferometric imaging of field-aligned plasma irregularities in the equatorial electrojet. *Geophysical Research Letters*, *18*(1), 41–44. https://doi.org/10.1029/90gl02603

Kudeki, E., & Woodman, R. F. (1990). A poststatistics steering technique for MST radar applications. *Radio Science*, *25*(4), 591–594. https://doi.org/10.1029/rs025i004p00591

Palmer, R. D., Gopalam, S., Yu, T., & Fukao, S. (1998). Coherent radar imaging using Capon's method. *Radio Science*, *33*(6), 1585–1598. https://doi.org/10.1029/98rs02200

Patra, A. K., Srinivasulu, P., Chaitanya, P. P., Rao, M. D., & Jayaraman, A. (2014). First results on low-latitude E and F region irregularities obtained using the Gadanki Ionospheric Radar Interferometer. *Journal of Geophysical Research Space Physics*, *119*(12). https://doi.org/10.1002/2014ja020604

Rodrigues, F. S., Moraes, A. O., & De Paula, E. R. (2012). Imaging equatorial spread F irregularities with the São Luís coherent backscatter radar interferometer. *Radio Science*, *47*(4). https://doi.org/10.1029/2011rs004929

Röttger, J., & Ierkic, H. M. (1985). Postset beam steering and interferometer applications of VHF radars to study winds, waves, and turbulence in the lower and middle atmosphere. *Radio Science*, *20*(6), 1461–1480. https://doi.org/10.1029/rs020i006p01461

Sinha, S., Sarma, T. V. C., & Regeena, M. L. (2017). Estimation of doppler profile using multiparameter cost function method. *IEEE Transactions on Geoscience and Remote Sensing*, *55*(2), 932–942. https://doi.org/10.1109/tgrs.2016.2616918

Srinivasulu, P., Rao, M. D., Yasodha, P., Kamaraj, P., & Patra, A. K. (2013). Wide Scanning HF Active Array Radar for ionospheric probing at NARL. *Proc. Int. Radar Symp. India (IRSI), 2013*. Retrieved from http://www.radarindia.com/irsi13papers/13-FP-150.pdf

Woodman, R. F. (1971). Inclination of the geomagnetic field measured by an incoherent scatter technique. *Journal of Geophysical Research Atmospheres*, *76*(1), 178–184. https://doi.org/10.1029/ja076i001p00178

Woodman, R. F. (1997). Coherent radar imaging: Signal processing and statistical properties. *Radio Science*, *32*(6), 2373–2391. https://doi.org/10.1029/97rs02017

Woodman, R. F., & La Hoz, C. (1976). Radar observations ofFregion equatorial irregularities. *Journal of Geophysical Research Atmospheres*, *81*(31), 5447–5466. https://doi.org/10.1029/ja081i031p05447

**Timiti Vamsi Krishna**
VIT-AP University,
School of Electronics Engineering (SENSE),
Andhra Pradesh 522237,
Amaravati,
India,
vamsi.21phd7121@vitap.ac.in
ORCID 0000-0001-8131-2249

**Ravindra Dhuli**
VIT-AP University,
School of Electronics Engineering (SENSE),
Andhra Pradesh 522237,
Amaravati,
India,
ravindra.d@vitap.ac.in
ORCID 0000-0003-2155-8508